THE JOURNAL OF PHYSICAL CHEMISTRY LETTERS
A JOURNAL OF THE AMERICAN CHEMICAL SOCIETY

pubs.acs.org/JPCL Letter

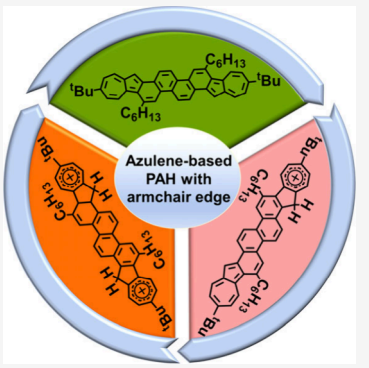
Linear Non-benzenoid Isomer of Acene Fusing Chrysene with Azulene Units

Peng Ren,[†] Liangliang Chen,[†] Chunlin Sun, Xinqiang Hua, Nan Luo, Baojin Fan, Pinyu Chen, Xiangfeng Shao, Hao-Li Zhang, and Zitong Liu*

Cite This: *J. Phys. Chem. Lett.* 2024, 15, 8410−8419 Read Online

ACCESS | Metrics & More | Article Recommendations | Supporting Information

ABSTRACT: Non-benzenoid polycyclic aromatic hydrocarbons (PAHs) have received considerable attention owing to their distinctive optical and electrical properties. Nevertheless, the synthesis and optoelectronic application of non-benzenoid PAHs remain challenging. Herein, we present a facile synthesis of linear non-benzenoid PAH with an armchair edge, **diACh**, by fusing chrysene with two azulene units. We systematically investigated the optical and electrical properties, which were also compared to its isomers, including benzenoid and non-benzenoid zigzag edge isomers. **diACh** exhibits global aromaticity, good planarity, and suitable highest occupied molecular orbital/lowest unoccupied molecular orbital energy levels. The protonation of **diACh** in solution successively forms a stable tropylium cation and dication. Moreover, the neutral, cationic, and dicationic states of **diACh** can be transformed with remarkable reversibility during the protonation−deprotonation process, as confirmed by ultraviolet−visible absorptions, fluorescence spectra, ^{1}H nuclear magnetic resonance, and theoretical calculations. Additionally, we fabricate p-type organic field-effect transistor (OFET) devices based on **diACh** with hole mobility up to 0.026 cm^2 V^{-1} s^{-1}, and we further develop OFET-based acid vapor sensors with good sensitivity, recyclability, and selectivity. These findings underscore the unique properties of linear non-benzenoid PAHs with an armchair edge engendered by the fusion of azulene with the acene backbone, showcasing prospective applications in organic optoelectronics.



Non-benzenoid polycyclic aromatic hydrocarbons (PAHs) have garnered significant attention owing to their distinctive (anti)aromaticity,[1−4] unique electron configurations,[5,6] and molecular orbital characteristics,[7,8] along with their potential applications in organic functional materials.[9−12] This arises from the partial substitution of hexagonal rings with pentagons or heptagons, commonly perceived as structure "defects", which are anticipated to modulate geometric configurations and electronic structures.[13−15]

Azulene stands as a seminal exemplar of non-benzenoid hydrocarbons, featuring a fused electron-rich pentagonal ring and an electron-deficient heptagonal ring with an inherent substantial dipole moment of 1.08 D.[16,17] This endows azulene with unique properties, including non-mirror-related Frontier molecular orbitals and anti-Kasha's fluorescence.[18−21] Furthermore, the electron-rich cyclopentadiene ring within azulene readily undergoes protonation, yielding a stable 6π-electron tropylium cation, thereby demonstrating notable proton responsiveness.[22] Therefore, the unique chemical and physical properties make azulene an ideal building block for constructing novel π-extended molecules, which have been applied in many areas, such as organic semiconductors,[23−27] single-molecular electronics,[28,29] and sensing and imaging.[30−34] Among them, non-benzenoid acenes with two fusing azulene units have gained a lot of attention.[35−40] For example, as shown in Scheme 1a, Zhang et al. reported diazulene-fused **DHR** as a non-benzenoid isomer of dibenzocoronene using the Scholl reaction and dehydrogenation.[38] **DHR** exhibited unusual S_0 to S_2 absorption and abnormal anti-Kasha S_2 to S_0 emission. Moreover, the single-crystal organic field-effect transistor (OFET) of **DHR** exhibited hole mobility up to 0.082 cm^2 V^{-1} s^{-1}. Liu et al. reported a series of diazulene-fused compounds (**BDA1**, **BDA2**, and **NDA**) as isomers of pentacene and hexacene using dehydration condensation, followed by Pd-catalyzed C−H coupling.[39] They exhibited narrow bandgaps with high stability in addition to protonation-caused enhanced near-infrared fluorescence. Ong et al. reported diazulene-fused **diAzA** as an isomer of heptacene.[40] The stability of the compound surpassed that of its corresponding isomer, while the oxidized dications of **diAzA** manifested an open-shell diradical character. These findings collectively underscore the distinctive physical properties exhibited by azulene-fused acenes relative to their benzenoid counterparts. Nonetheless, the scarcity of reported instances

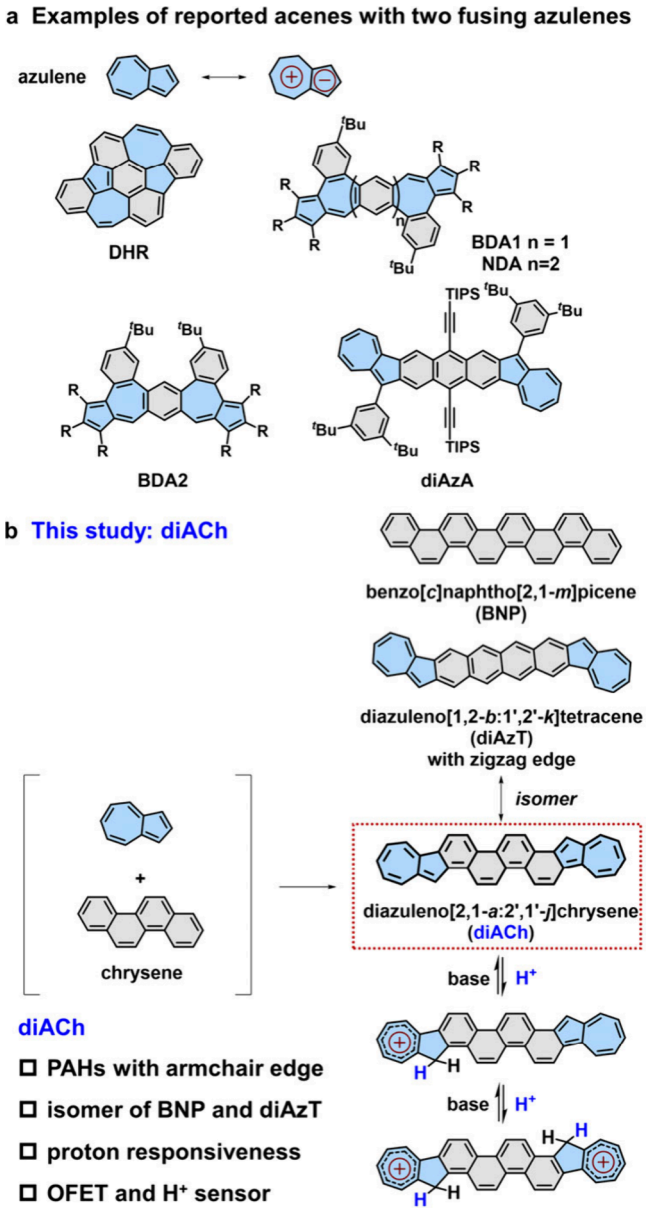
Received: June 29, 2024
Revised: July 31, 2024
Accepted: August 6, 2024

Downloaded via LANZHOU UNIV on August 22, 2024 at 00:42:27 (UTC).
See https://pubs.acs.org/sharingguidelines for options on how to legitimately share published articles.

ACS Publications © XXXX American Chemical Society

https://doi.org/10.1021/acs.jpclett.4c01917
J. Phys. Chem. Lett. 2024, 15, 8410−8419

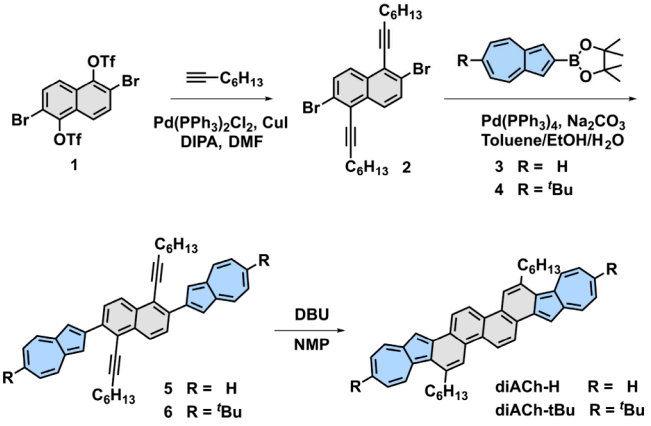
Scheme 1. (a) Examples of Reported Non-benzenoid Acenes with Two Azulene Units and (b) Design Rationale and Chemical Structure of diACh



involving azulene-fused acenes poses a limitation on their prospective applications, attributed to the synthetic challenges. Furthermore, most of the reported azulene-fused acenes have a zigzag edge, while those with an armchair edge are seldom reported.[37] Thus, the demand for new azulene-fused molecules with a facile synthetic method remains high to further elucidate their structure−property relationships.

This study presents a linear non-benzenoid acene with an armchair edge, termed diazuleno[2,1-*a*:2′,1′-*j*]chrysene (**diACh**), featuring two azulene units and one chrysene unit, which is an isomer of both **BNP** and non-benzenoid **diAzT** with a zigzag edge (Scheme 1b). Both **diACh-H** and **diACh-tBu** variants were synthesized via a straightforward method involving the key step of acetenyl 6-*endo* cyclization (Scheme 2). Crystal structural analysis and corresponding theoretical calculations of **diACh-tBu** reveal global aromaticity and good planarity, while **diAzT** with a zigzag edge exhibits an anti-

Scheme 2. Synthetic Routes to diACh-H and diACh-tBu



aromatic character at the seven-membered ring. Furthermore, upon protonation of neutral **diACh-tBu** with acid, a stable tropylium cation and dication are successively formed, of which the three show good reversible transformation under acid−base conditions, as corroborated by protonation-induced shifts in ultraviolet−visible (UV−vis) absorption bands, protonation-caused enhanced fluorescence, ^{1}H nuclear magnetic resonance (NMR) spectroscopy, and theoretical calculations. Leveraging this phenomenon, a ternary acid−base switch is constructed. It is noteworthy that the long-wavelength absorption maxima of protonated **diACh-tBu** exhibit obvious blue shifts compared to those of protonated **diAzT** with a zigzag edge, which is due to the electron transition across multiple energy levels of protonated **diACh-tBu** based on theoretical calculations. Additionally, considering the suitable highest occupied molecular orbital (HOMO) level (−5.01 eV), thin-film OFET devices based on **diACh-H** were fabricated, resulting in a hole mobility of up to 0.026 cm^2 V^{-1} s^{-1}. Notably, the device exhibits promising utility as an acid vapor sensor with excellent sensitivity, selectivity, and reversibility. These collective findings underscore the unique aromaticity imparted by fusing azulene with the acene backbone, suggesting potential applications in organic optoelectronics.

The general synthetic procedure of **diACh-H** and **diACh-tBu** is shown in Scheme 2, with comprehensive synthetic details and characterizations provided in the Supporting Information. Notably, hexyl chains were introduced into both **diACh** and tertiary butyl (^{t}Bu), which was additionally incorporated to **diACh-tBu** to enhance the solubilities in organic solvents. Initially, compound **2** was obtained with a yield of 61% using compound **1** and 1-octyne in the presence of $Pd(PPh_3)_2Cl_2$, CuI, and diisopropyl alcohol (DIPA) via Sonogashira coupling. The borate esters of compounds **3** and **4** were prepared according to the reported literature,[41] which were subsequently reacted with compound **2** to yield compounds **5** and **6** in yields of 89 and 76% via Suzuki coupling, respectively. Finally, with 1,8-diazabicyclo-[5.4.0]-undec-7-ene (DBU) as the base, **diACh-H** and **diACh-tBu** were achieved with moderate yields of 40 and 48%, respectively, through classic 6-*endo* cyclization.[42] All compounds underwent thorough characterization using ^{1}H and ^{13}C NMR and high-resolution mass spectrometry (HRMS) (see the Supporting Information). It is noteworthy that **diACh-H** exhibits markedly poor solubility in typical organic solvents at room temperature, whereas **diACh-tBu**, featuring two sterically

https://doi.org/10.1021/acs.jpclett.4c01917
J. Phys. Chem. Lett. 2024, 15, 8410−8419

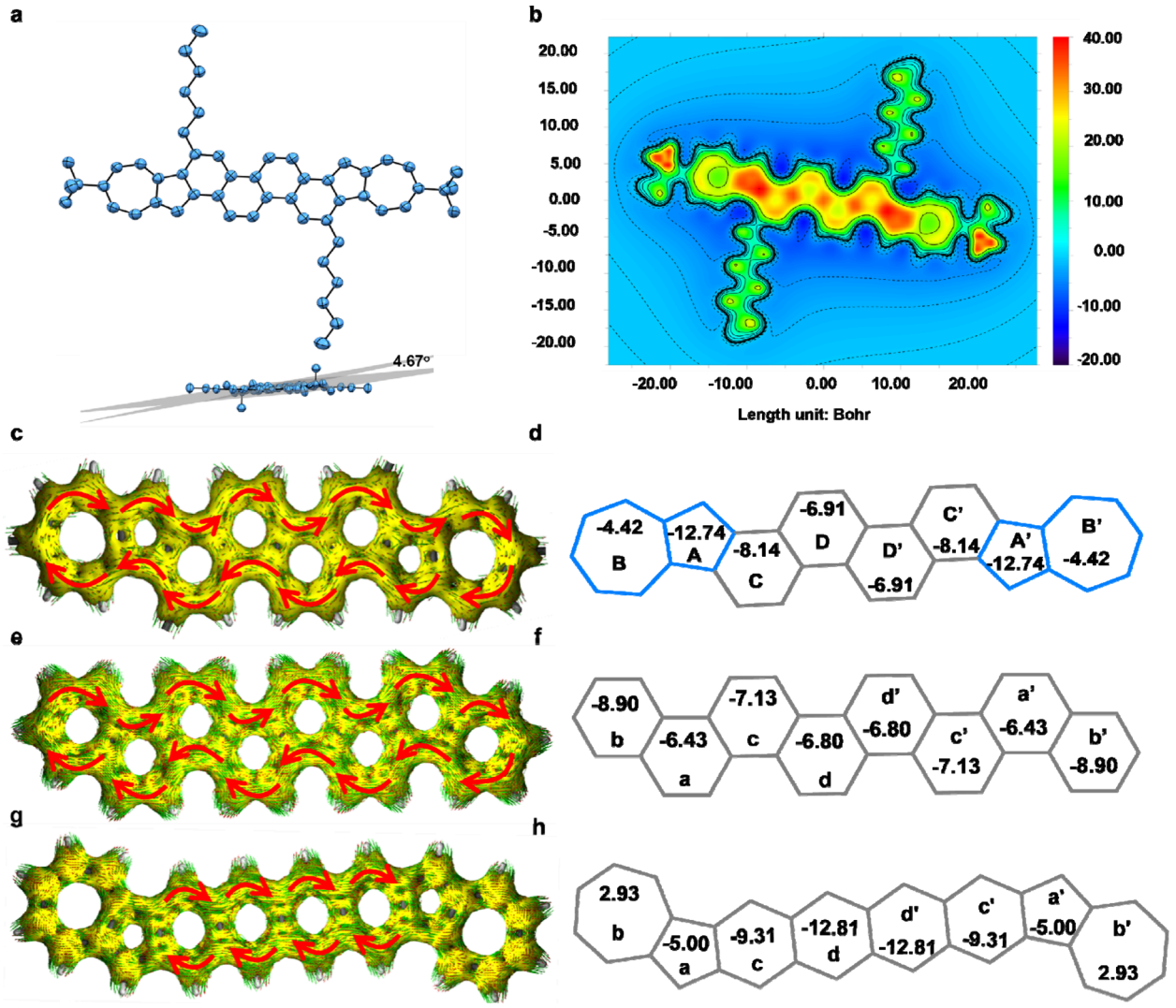


Figure 1. (a) Single-crystal structure of **diACh-tBu** (H was omitted for the sake of clarity). (b) ICSS at 2 Bohr of the z axis of **diACh-tBu**. The deep orange region shows strong aromaticity. (c, e, and g) Calculated ACID plots of (c) **diACh-tBu**, (e) **BNP**, and (g) **diAzT**. the clockwise ring currents are highlighted by red arrows under the magnetic field parallel to the z axis. (d, f, and h) Calculated NICS values of (d) **diACh-tBu**, (f) **BNP**, and (h) **diAzT**.

hindered ^{t}Bu groups, displays slight solubility in halogenated solvents, such as chloroform and 1,2-dichloroethane. For this, the measurements in solutions were performed on the basis of **diACh-tBu**, while the solid-state OFET devices and corresponding sensors were fabricated on the basis of **diACh-H** considering its lower steric hindrance, as discussed below.

Crystals of **diACh-tBu** suitable for single-crystal structural analysis were successfully obtained by gradually diffusing methanol into the chloroform solution. Consequently, the chemical structure of **diACh-tBu** was further elucidated through crystallographic analysis (Figure 1a and Table S1 of the Supporting Information). As shown in Figure 1a, the molecule exhibits good planarity, characterized by a small dihedral angle of 4.67° between two azulene units, indicative of potential charge transport behavior, as discussed below. Subsequent investigation of the π-stereoelectronic structure and aromaticity of **diACh-tBu** was conducted via theoretical calculations (panels b–d of Figure 1), encompassing anisotropy of the induced current density (ACID),[43] nucleus-independent chemical shift (NICS) analysis,[44] and an isotropic chemical shielding surface (ICSS) at 1 Å of the z axis.[45] As shown in Figure 1b, the ICSS map of **diACh-tBu** indicates a stronger shielding effect on the side of azulene's five-membered ring, while less shielding effect is found for the seven-membered ring. Additionally, the ACID plot reveals a clockwise ring current of the π electrons along the periphery, indicative of a trend toward global aromaticity (Figure 1c). For NICS, as shown in Figure 1d, the five-membered rings (A and A′) of **diACh-tBu** demonstrate pronounced aromaticity, as evidenced by the most negative NICS value of −12.74 ppm, while the NICS value of both seven-membered rings (B and B′) is only −4.42 ppm. The NICS values of other six-membered rings are −6.91 and −8.14 ppm in the middle (D and D′) and side positions (C and C′), respectively. For comparison, the ACID plot and NICS values of benzenoid isomer **BNP** and non-benzenoid isomer **diAzT** with a zigzag edge were also calculated (panels e–h of Figure 1). For **BNP**, the ACID plot also reveals a clockwise ring current of the π electrons along the periphery, indicative of a trend toward global aromaticity similar to that of **diACh-tBu** (Figure 1e). Nevertheless, the NICS values of **BNP** are in the region from −8.90 to −6.43, indicating a relatively uniform distribution of

https://doi.org/10.1021/acs.jpclett.4c01917
J. Phys. Chem. Lett. 2024, 15, 8410−8419

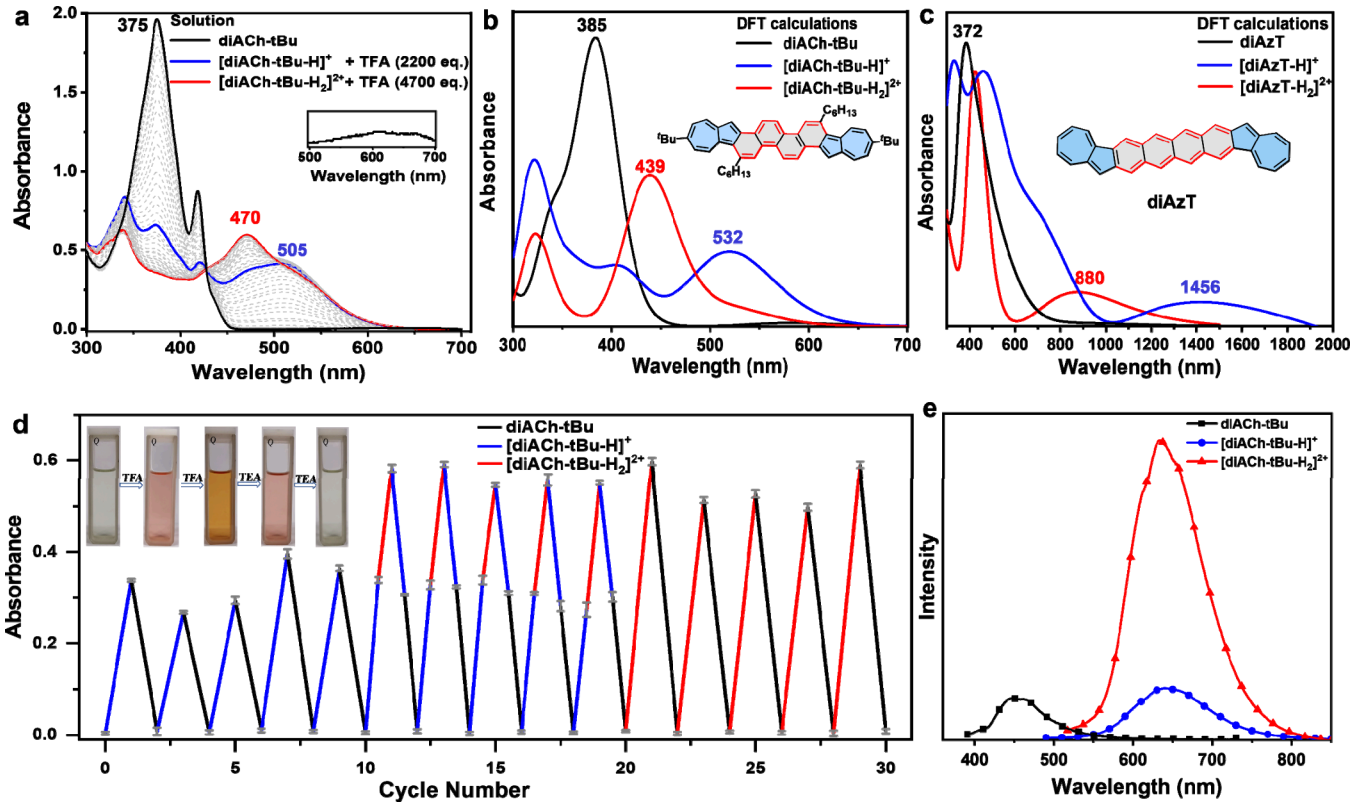


Figure 2. (a) UV−vis absorption of **diACh-tBu** by consecutively adding TFA in chloroform (1.13×10^{-5} mol/L). The inset is the enlarged *in situ* UV−vis absorption of **diACh-tBu** at 500−700 nm. (b) TD-DFT-calculated UV−vis absorption spectra of armchair edge **diACh-tBu**, [**diACh-tBu-H**]$^+$, and [**diACh-tBu-H$_2$**]$^{2+}$. (c) TD-DFT-calculated UV−vis absorption spectra of zigzag edge **diAzT**, [**diAZT-H**]$^+$, and [**diAZT-H$_2$**]$^{2+}$. (d) Reversible UV−vis absorption variations of protonation−deprotonation of **diACh-tBu** over 15 cycles by adding TFA and TEA. The absorption intensities were collected at wavelengths of 500 nm for **diACh-tBu**, 505 nm for [**diACh-tBu-H**]$^+$, and 470 nm for [**diACh-tBu-H$_2$**]$^{2+}$. Insets are photos of the solutions of **diACh-tBu**, [**diACh-tBu-H**]$^+$, and [**diACh-tBu-H$_2$**]$^{2+}$ under 365 nm light irradiation. (e) Fluorescence emission spectra of **diACh-tBu**, [**diACh-tBu-H**]$^+$. and [**diACh-tBu-H$_2$**]$^{2+}$ in chloroform solution (1.13×10^{-5} mol/L).

electrons (Figure 1f). For **diAzT** with a zigzag edge, it shows different trends like **diACh-tBu**. The ACID plot of **diAzT** shows a clockwise ring current of the π electrons along the periphery, except for both seven-membered rings (Figure 1g), which indicates an anti-aromatic character. In addition, the aromaticity of zigzag isomer **diAzT** primarily concentrates on tetracene. This is further demonstrated by NICS values, which show that both seven-membered rings of **diAzT** show positive values of 2.93. Moreover, the five-membered rings of **diAzT** show less negative NICS values of −5.00, indicating weaker aromaticity compared to those of **diACh-tBu**. These findings corroborate the global aromatic nature of the **diACh-tBu** skeleton, with delocalized electrons unevenly distributed due to the incorporation of the azulene unit, suggesting different physical properties compared to those of **BNP** and **diAzT**. Moreover, the heightened electron density in the two five-membered rings within **diACh-tBu** suggests the potential for multiple-protonation behavior.

We then investigated the solution UV−vis absorptions of **diACh-tBu** and its protonation−deprotonation behavior by adding trifluoracetic acid (TFA) and triethylamine (TEA), complemented by time-dependent density functional theory (TD-DFT) calculations at the TD-PBE0(D3)/6-311G(d) level (Figure 2). The TD-DFT calculations exhibit a good correlation with the initial UV−vis absorption of diACh-tBu and its distinct spectral alterations following protonation (panels a and b of Figure 2 and Figures S1−S6 and Tables S2−S4 of the Supporting Information). As shown in panels a and b of Figure 2, **diACh-tBu** displayed long-wavelength weak absorption at ∼600 nm, corresponding to the characteristic $S_0 \rightarrow S_1$ [HOMO → lowest unoccupied molecular orbital (LUMO)] transition of azulene (Figures 2b and 3).[46] The absorption maxima (λ_{max}) of **diACh-tBu** at 375 nm corresponds to the characteristic $S_0 \rightarrow S_2$ of azulene, primarily

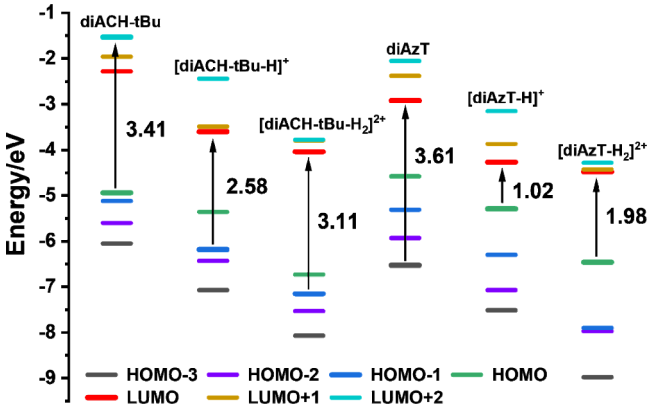


Figure 3. Schematic plot of calculated HOMO−LUMO energy levels of **diACh-tBu** and **diAzT** and their corresponding protonated compounds. The black arrows indicate the major transitions across energy levels of the corresponding major long-wavelength absorption maxima.

https://doi.org/10.1021/acs.jpclett.4c01917
J. Phys. Chem. Lett. 2024, 15, 8410−8419

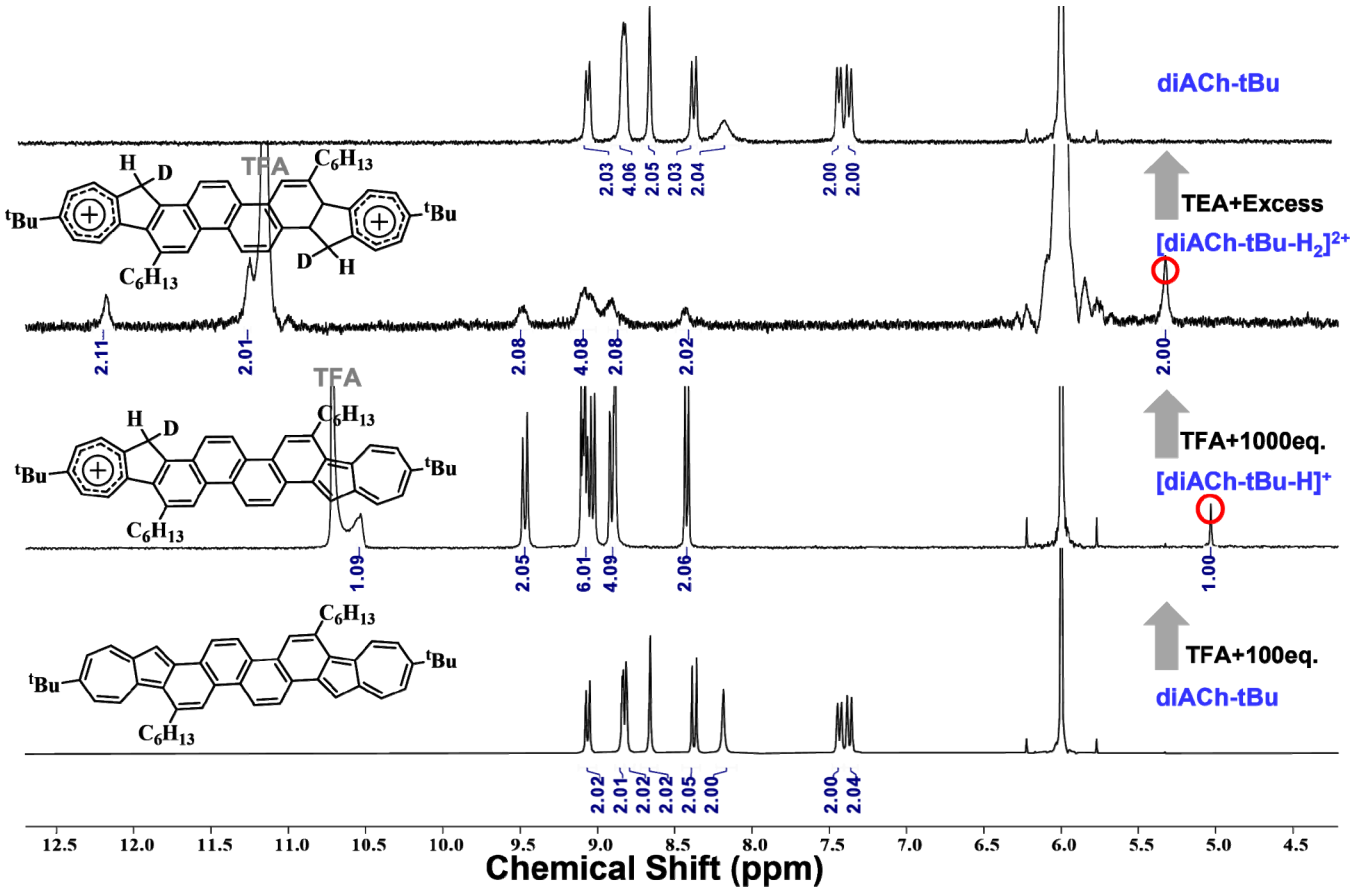


Figure 4. ^{1}H NMR spectra of **diACh-tBu**, [**diACh-tBu-H**]$^{+}$, and [**diACh-tBu-H$_2$**]$^{2+}$ in deuterotetrachloroethane ($C_2D_2Cl_4$) by *in situ* adding deuterated TFA to form [**diACh-tBu-H**]$^{+}$ and [**diACh-tBu-H$_2$**]$^{2+}$, respectively, and then TEA to restore.

attributed to the HOMO → LUMO+2 transition based on TD-DFT analysis. Subsequent addition of TFA to the **diACh-tBu** solution revealed nuanced spectral changes in the protonation process, with insignificant alterations observed at low TFA concentrations due to relatively insufficient electron density at the molecule's five-membered ring.[47] It is noted that the electron-rich positions with high proton affinity play a crucial role in azulene protonation.[48] With the increase of the TFA concentration until a ratio of 2200 equiv to **diACh-tBu**, the intensity of the main absorption peak at 375 nm diminished, while new absorption peaks emerged at 505, 420, and 341 nm and increased gradually. The major contributions can be attributed to HOMO−1 → LUMO, HOMO−1 → LUMO+3, and HOMO−1 → LUMO+2 of the tropylium cation [**diACh-tBu-H**]$^{+}$, respectively. Further addition of TFA leads to the formation of the tropylium dication [**diACh-tBu-H$_2$**]$^{2+}$. As shown in panels a and b of Figure 2, a new absorption peak at 470 nm appeared and increased gradually with adding TFA, attributed to HOMO−1 → LUMO based on TD-DFT. The isochromatic points observed at 502 and 338 nm correspond to optical differences associated with interconversion in the solution.

It is noteworthy that armchair edge **diACh-tBu** and corresponding tropylium (di)cations with chrysene of four six-membered rings exhibit an obvious blue shift in UV−vis absorptions compared to zigzag edge **BDA1**, **BDA2**, **NDA**, and **diAzA** with up to three six-membered rings (Scheme 1a).[39,40] For instance, the long-wavelength absorption maxima of **diAzA** and corresponding cation and dication with three fused six-membered rings are 386, 1775, and 1046 nm,[40] respectively, while those for **diACh-tBu**, [**diACh-tBu-H**]$^{+}$, and [**diACh-tBu-H$_2$**]$^{2+}$ are only 375, 505, and 470 nm, respectively, illustrating obviously different optical properties. For comparison, the absorptions of **diAzT** with a zigzag edge, the isomer of **diACh**, were also calculated (Figure 2c and Figures S7−S9 and Tables S5−S7 of the Supporting Information). In comparison to armchair edge **diACh-tBu** (Figure 2b), the long-wavelength absorption maxima of neutral **diAzT** shows a slight blue shift from 385 nm (**diACh-tBu**) to 372 nm, whereas the corresponding cation and dication are red-shifted to 1456 and 880 nm. It is found that the major absorption of neutral zigzag edge **diAzT** shows a blue shift compared to armchair edge **diACh-tBu**, whereas red shifts happen after protonation. This is due to the multiple energy level transitions for the neutral zigzag edge (**diAzT**) and protonated armchair edge [**diACh-tBu-H**]$^{+}$ and [**diACh-tBu-H$_2$**]$^{2+}$. As illustrated in Figure 3, neutral **diAzT** exhibits more multiple energy level transitions from HOMO−3 to LUMO than **diACh-tBu** (HOMO → LUMO+2), while [**diAzT-H**]$^{+}$ and [**diAzT-H$_2$**]$^{2+}$ exhibit a mono energy level transition from HOMO to LUMO compared to protonated **diACh-tBu** (HOMO−1 → LUMO). The experimental and theoretical results as well as previous reports[39,40] demonstrate the peculiar optical properties of the armchair structure of **diACh-tBu** compared to the zigzag edge structure. This is also proven by NICS calculations that protonation changes the NICS value of the five-membered ring from −12.74 in **diACh-tBu** to 1.07 in [**diACh-tBu-H**]$^{+}$ and 1.16 in [**diACh-tBu-H$_2$**]$^{2+}$, respectively. This is due to the

https://doi.org/10.1021/acs.jpclett.4c01917
J. Phys. Chem. Lett. 2024, 15, 8410−8419

different π-electron distribution of acene with zigzag and armchair edges, resulting in a different aromatic character (panels c−h of Figure 1).

Notably, these acid-mediated absorption changes of **diACh-tBu** are reversible, with spectral characteristics restored upon neutralization of the protonated species with TEA. As shown in Figure 2d, the protonation and deprotonation process between **diACh-tBu** and [**diACh-tBu-H**]$^+$, **diACh-tBu** and [**diACh-tBu-H$_2$**]$^{2+}$, and **diACh-tBu**, [**diACh-tBu-H**]$^+$, and [**diACh-tBu-H$_2$**]$^{2+}$, can be repeated for at least five consecutive cycles for each process, indicating excellent reversibility without significant spectral changes. In addition, the protonation and deprotonation process can also be observed through the naked eye under visible light. As shown in the inset of Figure 2d, the colors of **diACh-tBu**, [**diACh-tBu-H**]$^+$, and [**diACh-tBu-H$_2$**]$^{2+}$ are light green, pink, and claybank, respectively, showing a clear color distinction.

Furthermore, the protonation of **diACh-tBu** also induces alterations in its fluorescence emission properties. As shown in Figure 2e, the **diACh-tBu** solution exhibited a weak photoluminescence (PL) intensity with an emission wavelength maximum at 450 nm. Upon protonation to [**diACh-tBu-H**]$^+$, the emission wavelength maximum exhibited a red shift to 650 nm, while PL intensity was still weak. Nevertheless, upon further protonation to [**diACh-tBu-H$_2$**]$^{2+}$, a notable proton-induced PL intensity enhancement was observed with an emission wavelength maximum at 634 nm. This can also be observed under the naked eye. As shown in the inset of Figure 2e, the colors of **diACh-tBu**, [**diACh-tBu-H**]$^+$, and [**diACh-tBu-H$_2$**]$^{2+}$ are light green, crimson, and claybank, respectively, under UV light irradiation of 365 nm. Importantly, this process is also reversible. All of these suggest that the reversible protonation and deprotonation process of **diACh-tBu** can be used as a reversible ternary acid−base switch through UV−vis absorption spectra, fluorescence spectra, and even naked-eye observation under visible light and UV irradiation, respectively.

In situ ^{1}H NMR spectroscopy of **diACh-tBu** was performed by sequentially adding deuterated TFA and then TEA to further elucidate the protonation−deprotonation dynamics. As illustrated in Figure 4, the addition of TFA to **diACh-tBu** resulted in the formation of [**diACh-tBu-H**]$^+$ and [**diACh-tBu-H$_2$**]$^{2+}$, with subsequent restoration to **diACh-tBu** upon the addition of TEA. After TFA was added to **diACh-tBu**, a new chemical shift at 5.03 ppm emerged, attributed to the proton on the five-membered cation ring of [**diACh-tBu-H**]$^+$, which further downshifted to 5.32 ppm for [**diACh-tBu-H$_2$**]$^{2+}$. Additionally, the protons in the aromatic region on **diACh-tBu** exhibited a downshift following protonation with broadened signals observed upon the formation of the dication. Furthermore, the integrations of ^{1}H NMR of [**diACh-tBu-H**]$^+$ and [**diACh-tBu-H$_2$**]$^{2+}$ corresponded well with both chemical structures (Figure 4). These results further demonstrate that the protonation−deprotonation process is reversible. It should be noted that the concentration (4 mg/mL) of **diACh-tBu** for ^{1}H NMR measurement is much higher than that for UV−vis characterization (0.008 mg/mL; Figure 2a). The cation and dication transformations of ^{1}H NMR and UV−vis are different. The cation and dication transformations of ^{1}H NMR are faster than those in UV−vis spectra, indicating that the transformation is related to the **diACh-tBu** concentration.

In the following, we demonstrate that **diACh** can be used as an organic semiconductor for thin-film OFETs and the applications in OFET-based acid vapor sensors.[49,50] On the basis of cyclic voltammetry, the HOMO and LUMO energy levels of **diACh-tBu** were measured to be −5.01 and −3.04 eV, respectively (Figure S10 of the Supporting Information). Moreover, density functional theory (DFT) calculations at the level of B3LYP-6-31G were performed on the basis of crystallographic data of **diACh-tBu**. As shown in Figure S11 of the Supporting Information, the HOMOs are predominantly localized on the entire molecular skeleton, whereas the LUMOs are primarily distributed across the azulene units. The calculated HOMO and LUMO energies were determined to be −4.94 and −2.28 eV, respectively. For [**diACh-tBu-H**]$^+$, the HOMO is primarily distributed across neutral azulene and half of the chrysene unit, while the LUMO is primarily distributed on pronated azulene. The calculated HOMO and LUMO energy levels were −5.36 and −3.60 eV. For [**diACh-tBu-H$_2$**]$^{2+}$, the HOMO is primarily localized on the chrysene skeleton, while the LUMO is primarily distributed across the whole backbone. The HOMO and LUMO energy levels of [**diACh-tBu-H$_2$**]$^{2+}$ were calculated to be −6.73 and −4.04 eV. It should be mentioned that the HOMOs and LUMOs were all reduced after protonation, which may affect the charge transport upon protonation, thus realizing proton sensing, as discussed below. Notably, these values differ from those obtained with via cyclic voltammetry, which is understandable as solvent effects and intermolecular interactions are not considered in the theoretical calculations.[51] It should be mentioned that **diACh-tBu** selected for the above study is due to its better solubility than **diACh-H** in organic solvents. Nevertheless, **diACh-H** may show similar energy levels and planarity to those of **diACh-tBu**, considering that the only disparity lies in the substituent group (Scheme 2). Above all, the suitable HOMO levels of **diACh** suggest its suitability for application as a p-type organic semiconductor in OFETs.[52−56]

We fabricated bottom-gate bottom-contact (BG-BC) OFETs and corresponding acid vapor sensors utilizing **diACh-H**, devoid of the steric hindrance imparted by tertiary butyl groups. As shown in Figure 5a, the devices were prepared by vacuum deposition of **diACh-H** on the *n*-octadecyltrichlorosilane (OTS)-modified Si/SiO$_2$ substrate (for details, see the Supporting Information). The optimized vacuum-deposited temperature was determined to be 180 °C under a pressure of 10^{-4} bar. All devices were measured under ambient conditions. The typical transfer and output curves are depicted in Figure 5b and Figure S12 of the Supporting Information. The devices exhibited typical p-channel characteristics, with the maximum/average hole mobilities of 0.026/0.017 cm^2 V^{-1} s^{-1}, an on/off ratio of ∼10^8, and a threshold voltage of −6 V. To gain insights into the thin-film microstructures, atomic force microscopy (AFM) and grazing incidence wide-angle X-ray scattering (GIWAXS) analyses were performed. As shown in Figure S13 of the Supporting Information, the AFM image of a thin film of **diACh-H** exhibited interconnected thin microrods with uniform structures, while the root-mean-square roughness was calculated to be 1.14 nm, indicating flat thin-film morphologies. For the GIWAXS in Figure S14 of the Supporting Information, a series of obvious signals were found with a $\pi-\pi$ stacking distance of 3.36 Å, indicating robust crystallinities and dense packing order within the thin film.[57]

Given **diACh**'s proton responsiveness ability in solutions, we sought to investigate the potential of **diACh** as an electrical sensor for acid vapor. Therefore, OFET-based acid vapor sensors based on the azulene unit were first studied using

https://doi.org/10.1021/acs.jpclett.4c01917
J. Phys. Chem. Lett. 2024, 15, 8410−8419

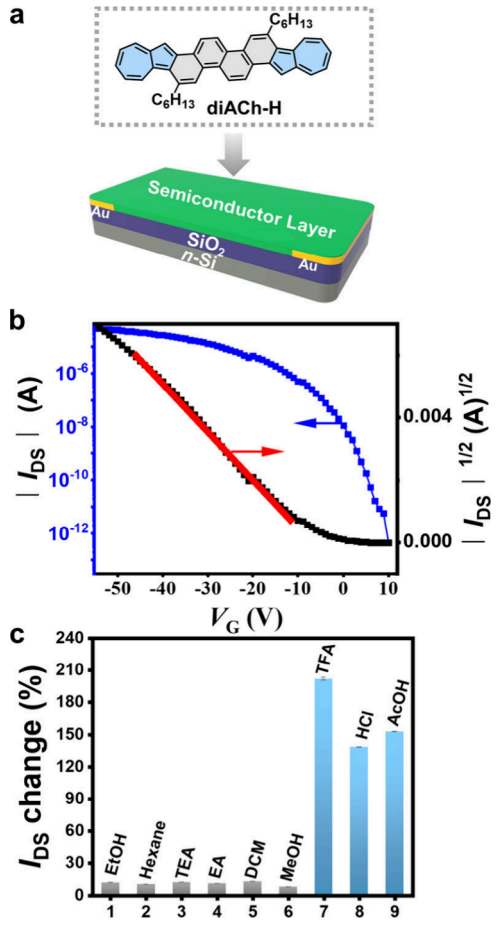


Figure 5. (a) Schematic illustration of OFET with BG-BC architecture. (b) Transfer characteristics of OFETs based on **diACh-H** (V_{DS} = −70 V, W = 1440 μm, and L = 5 μm). (c) Variation of the drain current after exposure to different gas vapors: EtOH (5000 ppm), hexane (5000 ppm), TEA (5000 ppm), EA (5000 ppm), DCM (5000 ppm), MeOH (5000 ppm), TFA (300 ppm), HCl (4000 ppm), and AcOH (5000 ppm).

gaseous analytes, which were prepared by controlling their volume relative to air to achieve different dilutions (for details, see the Supporting Information).[58,59] The source−drain current (I_{DS}) changes of FET devices were recorded following exposure to different concentrations of TFA ranging from 1 to 100 ppm, as shown in Figure S15 of the Supporting Information. Notably, I_{DS} increased and showed more obvious changes with the gradual increase in the TFA vapor concentration. For instance, I_{DS} altered by 10.3% after exposure to 1 ppm of TFA vapor, which was further increased by 82.5% after exposure to 50 ppm of TFA vapor. I_{DS} can be restored after exposure to air within 2 s. Therefore, the response of the OFET device featuring **diACh-H** demonstrates stable and reproducible responses to TFA, rendering it a sensitive acid vapor sensor. We notice that I_{DS} exhibits increases after exposure to acid vapor. This is in accordance with a previous report that the bulk conductivity of the azulene-containing polymer increases after introducing acid.[60] This should be due to the trace proton doping of the azulene unit, which causes charge transfer between the neutral and protonated molecule, ultimately increasing the intrinsic conductivity.[61] To demonstrate this, we calculated the stereoscopic electrostatic potential maps of **diACh-tBu** and corresponding protonated states based on the single-crystal structure. As shown in Figure S16 of the Supporting Information, **diACh-tBu** exhibits a uniform electrostatic potential distribution with a dipole moment of 0 D. After protonation, the charge density distributions are not uniform, with molecular dipole moments of 25.89 D for [**diACh-tBu-H**]$^+$ and 0.92 D for [**diACh-tBu-H$_2$**]$^{2+}$, resulting in intermolecular charge transfer. In addition to TFA, OFETs employing **diACh-H** were subjected to a variety of vapors of volatile solvents, including ethanol, *n*-hexane, TEA, ethyl acetate (EA), dichloromethane (DCM), methanol (MeOH), hydrochloric acid (HCl), and acetic acid (AcOH). As shown in Figure 5c, I_{DS} values showed obvious increases after exposure to acid vapor (HCl and AcOH), whereas the variations in I_{DS} remained relatively negligible for other vapors, even at high concentrations (5000 ppm). These results reveal that the OFET-based acid vapor sensor featuring **diACh-H** shows good sensitivity, recyclability, and selectivity.

In this study, we synthesized a new linear non-benzenoid isomer of acene, **diACh** with an armchair edge, by fusing chrysene with two azulene units via facile acetenyl 6-*endo* cyclization. The optical and electrical properties of **diACh** were investigated in detail as well as the differences with its benzenoid isomer **BNP** and corresponding zigzag edge structure **diAzT**. **diACh** shows good planarity and global aromaticity on the basis of crystallographic data. The UV−vis absorptions, fluorescence spectra, ^{1}H NMR spectroscopy, and TD-DFT calculations collectively indicate that **diACh** can be protonated to form the corresponding tropylium cation and consecutive dication under acid conditions, with reversible protonation−deprotonation capabilities. Apart from its optical attributes, we fabricate OFET devices based on **diACh** to explore its electrical properties, revealing the p-type transport behavior. In addition, new OFET-based acid vapor sensors are realized by synergistically utilizing the charge transport and protonation−deprotonation properties of **diACh**. The preliminary study positions **diACh** as a promising candidate for future applications in optoelectronics. Ongoing efforts have focused on enhancing the charge mobility of **diACh** through OFET device optimization as well as substituting more soluble alkyl linear side chains to improve its solution processability. In addition, the synthesis of new armchair edge non-benzenoid PAHs with more fused azulene units or six-membered rings is still in progress.

■ ASSOCIATED CONTENT

Supporting Information

The Supporting Information is available free of charge at https://pubs.acs.org/doi/10.1021/acs.jpclett.4c01917.

Full experimental details, NMR spectra, computational information, and crystallographic details (PDF)
Crystallographic Information File (CIF)
checkCIF/PLATON report (PDF)

■ AUTHOR INFORMATION

Corresponding Author

Zitong Liu − *State Key Laboratory of Applied Organic Chemistry, Key Laboratory of Special Function Materials and Structure Design, College of Chemistry and Chemical Engineering, Lanzhou University, Lanzhou, Gansu 730000, People's Republic of China;* orcid.org/0000-0003-1185-9219; Email: zitong_@iccas.ac.cn

https://doi.org/10.1021/acs.jpclett.4c01917
J. Phys. Chem. Lett. 2024, 15, 8410−8419

Authors

Peng Ren − *State Key Laboratory of Applied Organic Chemistry, Key Laboratory of Special Function Materials and Structure Design, College of Chemistry and Chemical Engineering, Lanzhou University, Lanzhou, Gansu 730000, People's Republic of China*

Liangliang Chen − *Sauvage Center for Molecular Sciences, College of Chemistry and Molecular Sciences, Wuhan University, Wuhan, Hubei 430072, People's Republic of China*

Chunlin Sun − *State Key Laboratory of Applied Organic Chemistry, Key Laboratory of Special Function Materials and Structure Design, College of Chemistry and Chemical Engineering, Lanzhou University, Lanzhou, Gansu 730000, People's Republic of China*

Xinqiang Hua − *State Key Laboratory of Applied Organic Chemistry, Key Laboratory of Special Function Materials and Structure Design, College of Chemistry and Chemical Engineering, Lanzhou University, Lanzhou, Gansu 730000, People's Republic of China*

Nan Luo − *State Key Laboratory of Applied Organic Chemistry, Key Laboratory of Special Function Materials and Structure Design, College of Chemistry and Chemical Engineering, Lanzhou University, Lanzhou, Gansu 730000, People's Republic of China*

Baojin Fan − *College of Chemistry and Chemical Engineering Institute of Polymers and Energy Chemistry, Nanchang University, Nanchang, Jiangxi 330031, People's Republic of China*

Pinyu Chen − *State Key Laboratory of Applied Organic Chemistry, Key Laboratory of Special Function Materials and Structure Design, College of Chemistry and Chemical Engineering, Lanzhou University, Lanzhou, Gansu 730000, People's Republic of China*

Xiangfeng Shao − *State Key Laboratory of Applied Organic Chemistry, Key Laboratory of Special Function Materials and Structure Design, College of Chemistry and Chemical Engineering, Lanzhou University, Lanzhou, Gansu 730000, People's Republic of China;* orcid.org/0000-0002-8710-4122

Hao-Li Zhang − *State Key Laboratory of Applied Organic Chemistry, Key Laboratory of Special Function Materials and Structure Design, College of Chemistry and Chemical Engineering, Lanzhou University, Lanzhou, Gansu 730000, People's Republic of China;* orcid.org/0000-0002-6322-5202

Complete contact information is available at: https://pubs.acs.org/10.1021/acs.jpclett.4c01917

Author Contributions

†Peng Ren and Liangliang Chen contributed equally to this work.

Notes

The authors declare no competing financial interest.

■ ACKNOWLEDGMENTS

This work was financially supported by the National Natural Science Foundation of China (NSFC, 22375080, 22175081, and 22075117), the State Key Laboratory of Physical Chemistry of Solid Surfaces (202108), the Open Foundation of State Key Laboratory of Electronic Thin Films and Integrated Devices (KFJJ202203), and the Beijing National Laboratory for Molecular Sciences (BNLM202010). The authors also thank Jing Yan from Modern Oriental (Beijing) Technology Development Co., Ltd. for helpful suggestion and the Supercomputing Center of Lanzhou University. A portion of this work is based on the data obtained at the BSRF-1W1A beamline. The authors gratefully acknowledge the cooperation of the beamline scientists at the BSRF-1W1A beamline.

■ REFERENCES

(1) Pun, S. H.; Miao, Q. Toward Negatively Curved Carbons. *Acc. Chem. Res.* **2018**, *51*, 1630−1642.

(2) Fei, Y.; Liu, J. Synthesis of Defective Nanographenes Containing Joined Pentagons and Heptagons. *Adv. Sci.* **2022**, *9*, 2201000.

(3) Ding, F.; Xia, D.; Sun, W.; Chen, W.; Yang, Y.; Lin, K.; Zhang, F.; Guo, X. Sulfer-Containing Bent N-Heteroacenes. *Chem. - Eur. J.* **2019**, *25*, 15106−15111.

(4) Liu, B.; Chen, M.; Liu, X.; Fu, R.; Zhao, Y.; Duan, Y.; Zhang, L. Bespoke Tailoring of Graphenoid Sheets: A Rippled Molecular Carbon Comprising Cyclically Fused Nonbenzenoid Rings. *J. Am. Chem. Soc.* **2023**, *145*, 28137−28145.

(5) Liu, R.; Fu, Y.; Wu, F.; Liu, F.; Zhang, J.-J.; Yang, L.; Popov, A. A.; Ma, J.; Feng, X. Modular Synthesis of Structurally Diverse Azulene-Embedded Polycyclic Aromatic Hydrocarbons by Knoevenagel-Type Condensation. *Angew. Chem., Int. Ed.* **2023**, *62*, No. e202219091.

(6) Qin, L.; Xie, J.; Wu, B.; Hong, H.; Yang, S.; Ma, Z.; Li, C.; Zhang, G.; Zhang, X.-S.; Liu, K.; Zhang, D. Axially Chiral Nonbenzenoid Nanographene with Second Harmonic Generation Property. *J. Am. Chem. Soc.* **2024**, *146*, 12206−12214.

(7) Jiang, W.; Wang, Z. Molecular Carbon Imides. *J. Am. Chem. Soc.* **2022**, *144*, 14976−14991.

(8) Hirai, M.; Tanaka, N.; Sakai, M.; Yamaguchi, S. Structurally Constrained Boron-, Nitrogen-, Silicon-, and Phosphorus-Centered Polycyclic π-Conjugated Systems. *Chem. Rev.* **2019**, *119*, 8291−8331.

(9) Xin, H.; Ge, C.; Jiao, X.; Yang, X.; Rundel, K.; McNeill, C. R.; Gao, X. Incorporation of 2,6-Connected Azulene Units into the Backbone of Conjugated Polymers: Towards High-Performance Organic Optoelectronic Materials. *Angew. Chem., Int. Ed.* **2018**, *57*, 1322−1326.

(10) Mathey, P.; Lirette, F.; Fernández, I.; Renn, L.; Weitz, R. T.; Morin, J.-F. Annulated Azuleno[2,1,8-*ija*]Azulenes: Synthesis and Properties. *Angew. Chem., Int. Ed.* **2023**, *62*, No. e202216281.

(11) Gu, P.-Y.; Wang, Z.; Zhang, Q. Azaacenes as Active Elements for Sensing and Bio Applications. *J. Mater. Chem. B* **2016**, *4*, 7060−7074.

(12) Chen, Y.; Zhao, Y.; Zhao, Y.; Chen, X.; Liu, X.; Li, L.; Cao, D.; Wang, S.; Zhang, L. A Novel Homoconjugated Propellane Triimide: Synthesis, Structural Analyses, and Gas Separation. *Angew. Chem., Int. Ed.* **2024**, *63*, No. e202401706.

(13) Qin, L.; Huang, Y.-Y.; Wu, B.; Pan, J.; Yang, J.; Zhang, J.; Han, G.; Yang, S.; Chen, L.; Yin, Z.; Shu, Y.; Jiang, L.; Yi, Y.; Peng, Q.; Zhou, X.; Li, C.; Zhang, G.; Zhang, X.-S.; Wu, K.; Zhang, D. Diazulenorubicene as a Non-benzenoid Isomer of *peri*-Tetracene with Two Sets of 5/7/5 Membered Rings Showing Good Semiconducting Properties. *Angew. Chem., Int. Ed.* **2023**, *62*, No. e202304632.

(14) Wang, L.; Peng, X.; Su, J.; Wang, J.; Gallardo, A.; Yang, H.; Chen, Q.; Lyu, P.; Jelínek, P.; Liu, J.; Wong, M. W.; Lu, J. Highly Selective On-Surface Ring-Opening of Aromatic Azulene Moiety. *J. Am. Chem. Soc.* **2024**, *146*, 1563−1571.

(15) Klein, B. P.; van der Heijden, N. J.; Kachel, S. R.; Franke, M.; Krug, C. K.; Greulich, K. K.; Ruppenthal, L.; Müller, P.; Rosenow, P.; Parhizkar, S.; Bocquet, F. C.; Schmid, M.; Hieringer, W.; Maurer, R. J.; Tonner, R.; Kumpf, C.; Swart, I.; Gottfried, J. M. Molecular Topology and the Surface Chemical Bond: Alternant Versus Nonalternant Aromatic Systems as Functional Structural Elements. *Phys. Rev. X* **2019**, *9*, 011030.

(16) Anderson, A. G.; Steckler, B. M. Azulene. VIII. A Study of the Visible Absorption Spectra and Dipole Moments of Some 1- and 1, 3-Substituted Azulenes. *J. Am. Chem. Soc.* **1959**, *81*, 4941−4946.
(17) Xin, H.; Hou, B.; Gao, X. Azulene-Based π-Functional Materials: Design, Synthesis, and Applications. *Acc. Chem. Res.* **2021**, *54*, 1737−1753.
(18) Michl, J.; Thulstrup, E. W. Why is Azulene Blue and Anthracene White? A Simple Mo Picture. *Tetrahedron* **1976**, *32*, 205−209.
(19) Viswanath, G.; Kasha, M. Confirmation of the Anomalous Fluorescence of Azulene. *J. Chem. Phys.* **1956**, *24*, 574−577.
(20) Beer, M.; Longuet-Higgins, H. C. Anomalous Light Emission of Azulene. *J. Chem. Phys.* **1955**, *23*, 1390−1391.
(21) Dunlop, D.; Ludvíková, L.; Banerjee, A.; Ottosson, H.; Slanina, T. Excited-State (anti)Aromaticity Explains Why Azulene Disobeys Kasha's Rule. *J. Am. Chem. Soc.* **2023**, *145*, 21569−21575.
(22) Danyluk, S. S.; Schneider, W. G. The Proton Resonance Spectra and Structures of Substituted Azulenes in Trifluoroacetic Acid. *Can. J. Chem.* **1962**, *40*, 1777−1785.
(23) Hou, B.; Li, J.; Zhou, Z.; Tan, W. L.; Yang, X.; Zhang, J.; McNeill, C. R.; Ge, C.; Wang, J.; Gao, X. Incorporation of Electron-Rich Indacenodithiophene Units into the Backbone of 2,6-Azulene-Based Conjugated Polymers for Proton-Responsive Materials and p-Type Polymeric Semiconductors. *ACS Mater. Lett.* **2022**, *4*, 392−400.
(24) Tang, T.; Kyaw, A. K. K.; Zhu, Q.; Xu, J. Water-dispersible Conducting Polyazulene and its Application in Thermoelectrics. *Chem. Commun.* **2020**, *56*, 9388−9391.
(25) Yamaguchi, Y.; Takubo, M.; Ogawa, K.; Nakayama, K.-i.; Koganezawa, T.; Katagiri, H. Terazulene Isomers: Polarity Change of OFETs through Molecular Orbital Distribution Contrast. *J. Am. Chem. Soc.* **2016**, *138*, 11335−11343.
(26) Puodziukynaite, E.; Wang, H.-W.; Lawrence, J.; Wise, A. J.; Russell, T. P.; Barnes, M. D.; Emrick, T. Azulene Methacrylate Polymers: Synthesis, Electronic Properties, and Solar Cell Fabrication. *J. Am. Chem. Soc.* **2014**, *136*, 11043−11049.
(27) Yao, J.; Cai, Z.; Liu, Z.; Yu, C.; Luo, H.; Yang, Y.; Yang, S.; Zhang, G.; Zhang, D. Tuning the Semiconducting Behaviors of New Alternating Dithienyldiketopyrrolopyrrole−Azulene Conjugated Polymers by Varying the Linking Positions of Azulene. *Macromolecules* **2015**, *48*, 2039−2047.
(28) Schwarz, F.; Koch, M.; Kastlunger, G.; Berke, H.; Stadler, R.; Venkatesan, K.; Lortscher, E. Charge Transport and Conductance Switching of Redox-Active Azulene Derivatives. *Angew. Chem., Int. Ed.* **2016**, *55*, 11781−11786.
(29) Cai, S.; Deng, W.; Huang, F.; Chen, L.; Tang, C.; He, W.; Long, S.; Li, R.; Tan, Z.; Liu, J.; Shi, J.; Liu, Z.; Xiao, Z.; Zhang, D.; Hong, W. Light-Driven Reversible Intermolecular Proton Transfer at SingleMolecule Junctions. *Angew. Chem., Int. Ed.* **2019**, *58*, 3829−3833.
(30) Lupu, S.; Lete, C.; Marin, M.; Totir, N.; Balaure, P. C. Electrochemical Sensors based on Platinum Electrodes Modified with Hybrid Inorganic−Organic Coatings for Determination of 4-Nitrophenol and Dopamine. *Electrochim. Acta* **2009**, *54*, 1932−1938.
(31) Teodorescu, F.; Lete, C.; Marin, M.; Munteanu, C.; Totir, N. A Novel Glucose Biosensor Based on Poly(azulene-co-3-thiophene acetic acid) Conducting Films. *Rev. Chim.* **2013**, *64*, 15−21.
(32) Zhou, Y.; Zou, Q.; Qiu, J.; Wang, L.; Zhu, L. Rational Design of a Green-Light-Mediated Unimolecular Platform for Fast Switchable Acidic Sensing. *J. Phys. Chem. Lett.* **2018**, *9*, 550−556.
(33) Zhou, Y.; Zhuang, Y.; Li, X.; Ågren, H.; Yu, L.; Ding, J.; Zhu, L. Selective Dual-Channel Imaging on Cyanostyryl-Modified Azulene Systems with Unimolecularly Tunable Visible−Near Infrared Luminescence. *Chem. - Eur. J.* **2017**, *23*, 7642−7647.
(34) Murfin, L. C.; Weber, M.; Park, S. J.; Kim, W. T.; Lopez-Alled, C. M.; McMullin, C. L.; Pradaux-Caggiano, F.; Lyall, C. L.; Kociok-Köhn, G.; Wenk, J.; Bull, S. D.; Yoon, J.; Kim, H. M.; James, T. D.; Lewis, S. E. Azulene-Derived Fluorescent Probe for Bioimaging: Detection of Reactive Oxygen and Nitrogen Species by Two-Photon Microscopy. *J. Am. Chem. Soc.* **2019**, *141*, 19389−19396.
(35) Toda, T.; Shimazaki, N.; Mukai, T.; Kabuto, C. Synthesis and Physical Properties of 6,12-Diarylazuleno[1,2-b]Azulenes. *Tetrahedron Lett.* **1980**, *21*, 4001−4004.
(36) Kuroda, S.; Hirooka, S.; Iwaki, H.; Ikeda, M.; Nakao, T.; Ogisu, M.; Yasunami, M.; Takase, K. Synthesis of Methyl Azulen[1,2-b]Azulene-2-Carboxylate and Dimethyl Azulen[1,2-b]Azulene-2,4-Dicarboxylate. *Chem. Lett.* **1986**, *15*, 2039−2042.
(37) Razus, A. C. Syntheses of Azulene Embedded Polycyclic Compounds. *Symmetry* **2024**, *16*, 382.
(38) Zhang, X. S.; Huang, Y. Y.; Zhang, J.; Meng, W.; Peng, Q.; Kong, R.; Xiao, Z.; Liu, J.; Huang, M.; Yi, Y.; Chen, L.; Fan, Q.; Lin, G.; Liu, Z.; Zhang, G.; Jiang, L.; Zhang, D. Dicyclohepta[ijkl,uvwx]-Rubicene with Two Pentagons and Two Heptagons as a Stable and Planar Non-benzenoid Nanographene. *Angew. Chem., Int. Ed.* **2020**, *59*, 3529−3533.
(39) Wang, S.; Tang, M.; Wu, L.; Bian, L.; Jiang, L.; Liu, J.; Tang, Z.-B.; Liang, Y.; Liu, Z. Linear Nonalternant Isomers of Acenes Fusing Multiple Azulene Units. *Angew. Chem., Int. Ed.* **2022**, *61*, No. e202205658.
(40) Ong, A.; Tao, T.; Jiang, Q.; Han, Y.; Ou, Y.; Huang, K.-W.; Chi, C. Azulene-Fused Acenes. *Angew. Chem., Int. Ed.* **2022**, *61*, No. e202209286.
(41) Lu, Y.; Qiao, Y.; Xue, H.; Zhou, G. From Colorless to Near-Infrared S-Heteroarene Isomers: Unexpected Cycloaromatization of Cyclopenta[b]Thiopyran Catalyzed by $PtCl_2$. *Org. Lett.* **2018**, *20*, 6632−6635.
(42) Aguilar, E.; Sanz, R.; Fernandez-Rodriguez, M. A.; Garcia-Garcia, P. 1,3-Dien-5-ynes: Versatile Building Blocks for the Synthesis of Carbo- and Heterocycles. *Chem. Rev.* **2016**, *116*, 8256−8311.
(43) Geuenich, D.; Hess, K.; Koehler, F.; Herges, R. Anisotropy of the Induced Current Density (ACID), A General Method to Quantify and Visualize Electronic Delocalization. *Chem. Rev.* **2005**, *105*, 3758−3772.
(44) Chen, Z.; Wannere, C. S.; Corminboeuf, C.; Puchta, R.; Schleyer, P. R. Nucleus-Independent Chemical Shifts (NICS) as an Aromaticity Criterion. *Chem. Rev.* **2005**, *105*, 3842−3888.
(45) Liu, P.; Chen, X.-Y.; Cao, J.; Ruppenthal, L.; Gottfried, J. M.; Müllen, K.; Wang, X.-Y. Revisiting Acepleiadylene: Two-Step Synthesis and π-Extension toward Nonbenzenoid Nanographene. *J. Am. Chem. Soc.* **2021**, *143*, 5314−5318.
(46) Jiang, Q.; Tao, T.; Phan, H.; Han, Y.; Gopalakrishna, T. Y.; Herng, T. S.; Li, G.; Yuan, L.; Ding, J.; Chi, C. Diazuleno-*s*-indacene Diradicaloids: Syntheses, Properties, and Local (anti)Aromaticity Shift from Neutral to Dicationic State. *Angew. Chem., Int. Ed.* **2018**, *57*, 16737−16741.
(47) Gao, H.; Ge, C.; Hou, B.; Xin, H.; Gao, X. Incorporation of 1,3-Free-2,6-Connected Azulene Units into the Backbone of Conjugated Polymers: Improving Proton Responsiveness and Electrical Conductivity. *ACS Macro Lett.* **2019**, *8*, 1360−1364.
(48) Wang, X.; Ng, J. K.-P.; Jia, P.; Lin, T.; Cho, C. M.; Xu, J.; Lu, X.; He, C. Synthesis, Electronic, and Emission Spectroscopy, and Electrochromic Characterization of Azulene−Fluorene Conjugated Oligomers and Polymers. *Macromolecules* **2009**, *42*, 5534−5544.
(49) Luo, L.; Liu, Z. Recent Progress in Organic Field-Effect Transistor-based Chem/Bio-Sensors. *View* **2022**, *3*, 20200115.
(50) Lin, P.; Yan, F. Organic Thin-Film Transistors for Chemical and Biological Sensing. *Adv. Mater.* **2012**, *24*, 34−51.
(51) Chen, X.; Wang, J.; Zhang, G.; Liu, Z.; Xu, W.; Zhang, D. New Core-Expanded Naphthalene Diimides with Different Functional Groups for Air-stable Solution-Processed Organic n-type Semiconductors. *New J. Chem.* **2013**, *37*, 1720−1727.
(52) Wang, C.; Dong, H.; Hu, W.; Liu, Y.; Zhu, D. Semiconducting π-Conjugated Systems in Field-Effect Transistors: A Material Odyssey of Organic Electronics. *Chem. Rev.* **2012**, *112*, 2208−2267.
(53) Chen, J.; Zhang, W.; Wang, L.; Yu, G. Recent Research Progress of Organic Small-Molecule Semiconductors with High Electron Mobilities. *Adv. Mater.* **2023**, *35*, 2210772.

https://doi.org/10.1021/acs.jpclett.4c01917
J. Phys. Chem. Lett. 2024, 15, 8410−8419

(54) Zhao, Y.; Wang, W.; He, Z.; Peng, B.; Di, C.-A.; Li, H. High-performance and multifunctional organic field-effect transistors. *Chin. Chem. Lett.* **2023**, *34*, 108094.
(55) Chen, L.; Wu, B.; Qin, L.; Huang, Y.-Y.; Meng, W.; Kong, R.; Yu, X.; ChenChai, K.; Li, C.; Zhang, G.; Zhang, X.-S.; Zhang, D. A perylene five-membered ring diimide for organic semiconductors and π-expanded conjugated molecules. *Chem. Commun.* **2022**, *58*, 5100−5103.
(56) Liu, J.; Hu, W.; Jiang, L. Monolayer Molecular Crystals and Devices. *Sci. Bull.* **2023**, *68*, 1474−1477.
(57) Zhang, C.; Tan, W. L.; Liu, Z.; He, Q.; Li, Y.; Ma, J.; Chesman, A. S. R.; Han, Y.; McNeill, C. R.; Heeney, M.; Fei, Z. High-Performance Unipolar n-Type Conjugated Polymers Enabled by Highly Electron-Deficient Building Blocks Containing F and CN Groups. *Macromolecules* **2022**, *55*, 4429−4440.
(58) Levitsky, I.; Krivoshlykov, S. G.; Grate, J. W. Rational Design of a Nile Red/Polymer Composite Film for Fluorescence Sensing of Organophosphonate Vapors Using Hydrogen Bond Acidic Polymers. *Anal. Chem.* **2001**, *73*, 3441−3448.
(59) Wang, Z.; Liu, Z.; Chen, L.; Yang, Y.; Ma, J.; Zhang, X.; Guo, Y.; Zhang, G.; Zhang, D. Highly Sensitive Field-Effect Ammonia/Amine Sensors with Low Driving Voltage Based on Low Bandgap Polymers. *Adv. Electron. Mater.* **2018**, *4*, 1800025.
(60) Wang, F.; Lai, Y.-H.; Han, M.-Y. Stimuli-Responsive Conjugated Copolymers Having Electro-Active Azulene and Bithiophene Units in the Polymer Skeleton: Effect of Protonation and p-Doping on Conducting Properties. *Macromolecules* **2004**, *37*, 3222−3230.
(61) Zhen, Y.; Inoue, K.; Wang, Z.; Kusamoto, T.; Nakabayashi, K.; Ohkoshi, S.-i.; Hu, W.; Guo, Y.; Harano, K.; Nakamura, E. Acid-Responsive Conductive Nanofiber of Tetrabenzoporphyrin Made by Solution Processing. *J. Am. Chem. Soc.* **2018**, *140*, 62−65.

https://doi.org/10.1021/acs.jpclett.4c01917
J. Phys. Chem. Lett. 2024, 15, 8410−8419